Sustainable Materials and Technologies 41 (2024) e01068

Contents lists available at ScienceDirect

Sustainable Materials and Technologies

journal homepage: www.elsevier.com/locate/susmat

Dual single atoms (Pt, Ni) and Pt—Ni alloy nanoparticles encapsulated N-doped carbon framework for durable ORR and HER electrocatalysts

Thanh Duc Le, Dong-Seog Kim, Geun-Jae Oh, Gi-Seung Shin, Tuong Van Tran, Byung-Guk Ahn, Yeon-Tae Yu *

Division of Advanced Materials Engineering, Research Center for Advanced Materials Development, Jeonbuk National University, Jeonju, 54896, South Korea

ARTICLE INFO

Keywords:
ZIF
Single atoms
Alloy nanoparticles
Oxygen reduction reaction
Hydrogen evolution reaction
Bifunctional electrocatalyst

ABSTRACT

High-activity, stable, and high-efficiency bifunctional Pt-based catalysts that promote oxygen reduction reactions (ORRs) and hydrogen evolution reactions (HERs) are urgently needed to meet the ever-intensifying energy demands. In this paper, we propose a novel strategy for enhancing an electrocatalyst's durability using a high-porosity and abundantly nitrogen-doped carbon framework (NDCF) support derived from ZIF-8. Pt—Ni alloy nanoparticles (NPs) surrounded by dense dual single atoms (SAs) of Pt and Ni were immobilized in a porous NDCF matrix ($PtNi_{SA\text{-}NPs}$/NDCF), synergistically exhibiting bifunctional catalytic activity and durability toward ORR and HER. Under acidic conditions, the $PtNi_{SA\text{-}NPs}$/NDCF exhibits a half-wave potential of 0.91 V and a favorable 4-electron pathway for ORR. It also displays an overpotential of 24.7 mV at a current density of 10 mA cm^{-2} and a mass activity of 6.1 A mg_{Pt}^{-1} (at 40 mV), indicating ultrahigh electrocatalytic activity for HER. Critically, the $PtNi_{SA\text{-}NPs}$/NDCF showed remarkable durability over 10,000 CV cycles, reducing ORR's half-wave potential by only 4 mV and HER's overpotential by a mere 6 mV at 10 mA cm^{-2}. We attribute this enhancement in durability to the stable graphitic carbon shell encapsulating the Pt—Ni alloy NPs and the enrichment of pyridinic-N coordination by the NDCF support.

1. Introduction

Pt-based catalysts are demonstrated to be among of the most effective electrocatalysts for oxygen reduction reactions (ORRs) in fuel cells and hydrogen evolution reactions (HERs) in regeneration fuel cells [1,2]. Unfortunately, their high cost, poor stability under harsh conditions, and associated with complicated manufacturing process have prevented them from large scale applications [3–6]. Means of reducing the amount of Pt used, such as improving Pt utilization and enhancing the stability of Pt-based catalysts, are top priorities [7–9]. The recent development of single-atom (SA) catalysts with (an ideal) 100% atomic utilization rate has attracted the attention of researchers and industrial engineers [10,11]. When tested, a uniform and dense distribution of Pt SA on the support material (e.g., carbon or metal oxide), Pt SA often shows better ORR catalytic performance than its bulk counterpart [12–14]. However, most Pt SA catalysts are reported to produce H_2O_2 through the $2e^-$ pathway rather than the $4e^-$ pathway for H_2O, as the breaking of the O—O bond is dynamically unfavorable on isolated Pt SA [15,16]. In fact, very few Pt SA catalysts have been reported to display $4e^-$ ORR selectively. Notably, these studies have ignored the role of concomitant Pt nanoparticles (NPs) that may contribute to catalytic performance [17,18]. As reported, pairing Pt SA with a suitable secondary metal atom to construct well-defined Pt-M dual-site SA catalysts or coordinated with nitrogen-doped carbon improves the activity and selectivity of Pt SA materials [19–21]. The enhanced catalytic activity of this Pt-M dual-site SA may be due to the electron transfer that occurs between heterogeneous atoms, which magnifies adsorption/desorption ability and reduces the energy barriers to an electrocatalytic reaction [22,23]. In addition, alloying Pt with transition metals (e.g., Pt—Ni, Pt—Co, Pt—Fe, Pt—Cu) delivers a significant improvement in intrinsic activity [24]. Moreover, in the harsh condition, transition metals are easily leached from Pt-based alloy NPs, leading a dramatic decrease in catalyst activity [25,26]. During the past decades, many efforts have been made to enhance the durability of Pt-based alloy catalysts via a phase transition from highly ordered Pt-M alloy to noble-rich core-shell structure or by coating the surface of Pt-M NPs with a carbon layer [27–29]. Among these, graphitic carbon layers can effectively improve the structural stability of the catalysts by preventing aggregation and

* Corresponding author.
E-mail address: yeontae@jbnu.ac.kr (Y.-T. Yu).

https://doi.org/10.1016/j.susmat.2024.e01068
Received 23 July 2023; Received in revised form 29 May 2024; Accepted 1 July 2024
Available online 27 July 2024
2214-9937/© 2024 Elsevier B.V. All rights are reserved, including those for text and data mining, AI training, and similar technologies.

migration due to Ostwald ripening through physical confinement during the electrocatalyst process [29].

Zeolitic imidazolate frameworks (ZIFs) have been shown to be suitable for preparation of nanoporous carbon-based supports for ORR and HER due to their large specific surface areas, tunable channels, and abundance of nitrogen [30,31]. During pyrolysis, 2-methylimidazole decomposes from its parent molecules to form a nitrogen-doped carbon framework (NDCF), which possesses enhanced structural properties, charge transport, and stability. In addition, metal heteroatoms (Pt, Pd, Ni, Mn, Fe, Co) can be evenly incorporated into the carbon matrix to generate more catalytic active sites for ORR and HER [32,33]. This is a result of the synergistic effects between the guest (metal atoms) and host (NDCF) driven by strong metal-N_x coordination, high specific surface area, and excellent electrical conductivity [31,34]. Importantly, some metals with low boiling points (such as zinc) can be evaporated during a high-temperature carbonization process, thereby enabling more pores and pathways by which reactants can access to the active sites [35]. Wang et al. has prepared a uniformly dispersed Fe-N_x-C electrocatalyst from ZIF-8 by a one-step pyrolysis method that not only improved ORR activity, but also possessed a high degree of graphitization that enhances conductivity and durability [36]. Liang et al. evenly immobilized Pt NPs on Co SA-ZIF-NC across multiple active sites, significantly improving the ORR and HER catalytic activity [37]. These works highlight the crucial role of pyridinic-N in enhancing the electrocatalytic activity of SA catalysts. Pyridinic-N has been reported to serve as anchoring sites for stabilizing single metallic atoms, modulating electronic properties, and facilitating the reaction pathway [38–40]. Such research, which explores new strategies that incorporate advanced architectures, maximizes the activity and durability of catalysts. In our previous work, dual SAs (Pt, Ni) and Pt—Ni alloy NPs were hybridized on an N-doped carbon support, and a synergistic effect resulted in improved catalyst activity toward ORR [41]. To meet the industrial-scale requirements, however, this catalyst's durability is required to be further improved [42].

In this paper, we introduce a novel electrocatalyst hybridizing Pt—Ni dual single atoms (Pt, Ni) and Pt—Ni alloy NPs anchored in NDCF, denoted as $PtNi_{SA\text{-}NPs}$/NDCF, derived from ZIF-8. The as-prepared NDCF support delivers an enhanced surface area that enriches intrinsic active sites and maximizes the anchorage of SAs and uniform distribution of Pt—Ni alloy NPs, thereby ensuring the occurrence of the catalytic reaction. In acidic media, the synthesized $PtNi_{SA\text{-}NPs}$/NDCF catalyst exhibits excellent electrocatalytic activity and remarkable durability toward ORR and HER. The enhanced durability, which significantly improves the chemical stabilization of $PtNi_{SA\text{-}NPs}$/NDCF, is attributed to the abundance of pyridinic-N coordinates and the highly porous structure of the NDCF support.

2. Experimental

2.1. Materials

Platinum (II) acetylacetonate ($Pt(acac)_2$, 97%), nickel (II) acetylacetonate ($Ni(acac)_2$, $\geq$ 98%), 2-Methylimidazole (2-MIM, 99%), and zinc nitrate hexahydrate ($Zn(NO_3)_2{\cdot}6H_2O$, 98%) were purchased from Sigma-Aldrich. Ethanol (C_2H_5OH, 99.5%) and acetone (CH_3COCH_3, 99.5%) were obtained from Samchun. Methanol (CH_3OH, 99.8%) were from Junsei. Ultrapure water (18.2 MW) was prepared by reverse osmosis followed by ion-exchange and filtration. The commercial Pt on Vulcan XC-72 (Pt/C, 20%) catalyst was obtained from Premetek. All chemicals were used as delivered without any pretreatment.

2.2. Synthesis of ZIF-8

ZIF-8 was synthesized by using the modification of a method that has been reported elsewhere [43]. Briefly, 2.79 g of $Zn(NO_3)_2{\cdot}6H_2O$ was completely dissolved in 70 mL of methanol (solution 1). 3.08 g of 2-methylimidazole was dissolved in 30 mL of methanol to form a homogenous solution (solution 2). Solution 1 was then added dropwise to solution 2 under sonication for 5 min at room temperature. The mixed solution was stirred constantly at room temperature for 4 h to form ZIF-8. The obtained white product was collected by centrifugation and washed for 3 times with methanol, then dried overnight in the freeze vacuum dryer.

2.3. Synthesis of N-doped carbon framework (NDCF)

The NDCF was prepared by carbonization of ZIF-8. The as-prepared ZIF-8 was pyrolyzed at 900 °C under an Ar atmosphere in a tube furnace for 3 h with the ramping rate of 5 °C/min. Then, the product was naturally cooled down to room temperature. Due to the low melting point of the Zn species, most can be evaporated at 900 °C; this leads to the formation the ultra-porous structure [44–46]. The obtained black powder is hereafter donated as NDCF.

2.4. Synthesis of $PtNi_{SA\text{-}NPs}$/NDCF, $Pt_{SA\text{-}NPs}$/NDCF and $Ni_{SA\text{-}NPs}$/NDCF

Following a typical protocol for the preparation of $PtNi_{SA\text{-}NPS}$/NDCF, 50 mg of as prepared NDCF was dispersed in the mixture solution that consisted of 25 mL of H_2O and 25 mL of ethanol, followed by sonication at room temperature for 1 h. Then, 1.5 mL of $Pt(acac)_2$ (6.5 mM in acetone solution) and 1.5 mL of $Ni(acac)_2$ (6.5 mM in ethanol solution) were added dropwise into this suspension under sonication over 1 h. After vigorous stirring at 80 °C for 24 h, the obtained suspension was freeze dried in vacuum at atmosphere overnight. The as-prepared metal ions encapsulated in the NDCF were pyrolyzed under Ar atmosphere in a tube furnace. The powder was heated to 900 °C at a heating rate of 5 °C/min and then maintained at 900 °C for 1 h. The corresponding sample was denotated as $PtNi_{SA\text{-}NPs}$/NDCF. For comparison, $Pt_{SA\text{-}NPs}$/NDCF and $Ni_{SA\text{-}NPs}$/NDCF, which have the same metal loading amount, were prepared by pyrolysis of Pt^{2+} or Ni^{2+} encapsulated NDCF, respectively.

2.5. Physical characterizations

TEM data was collected using a CS-corrected transmission electron microscope (CS-TEM) (JEM-2010, JEOL, USA) with an accelerating voltage of 200 kV held at the Korea Basic Science Institute, Jeonju center. The chemicals composition of the catalysts was examined by inductively coupled plasma spectrometry (ICPS) (ICPS-7500, Shimadzu Co., Japan). To dissolve the Pt and Ni elements, the catalyst was treated with aqua regia solution at 150 °C for 12 h and then filtered. The crystal structure of the synthesized catalyst was analyzed by X-ray diffraction (XRD) (Max 2005, Rigaku, Japan) using CuKα radiation (l = 1.54178 Å). Data was collected from 30° to 80° of 2θ degree, with a scanning speed of 0.5°/min and a step size of 0.02°. X-ray photoelectron spectroscopy (XPS) (Thermo Fisher Scientific, Multilab 2000, USA) was performed using monochromated Al Kα X-ray photon (hυ = 1486.6 eV) sources to determine the chemical states of each element's surface. A Tristar 3000 system (Micromeritics, Norcross, GA, USA), were used to perform the Brunauer-Emmett-Teller (BET) analysis to determine the specific surface area of the samples.

2.6. Electrochemical characterizations

The electrochemical catalytic activity of the prepared catalysts was assessed using a 3-electrode system connected to a potentiostat (Gamry instruments, Reference 3000 Potentistat/Galvanostat/ZRA, USA). A glassy carbon (GC) rotating disk electrode (RDE) with an active area of 0.196 cm^2 served as the working electrode. Ag/AgCl (saturated KCl solution) and a graphitic carbon rod were used as reference and counter electrodes, respectively. The catalyst inks were formed by dispersing 5 mg of catalyst powder in a solution containing 950 mL of ethanol and 50 mL of 5 wt% of Nafion solution during ultra-sonication for 1 h to obtain a homogeneous suspension. 10 mL of the catalyst ink ($\sim$ 2.5 mg_{Pt} cm^{-2})

was then dropped onto the surface of the GC-RDE. The commercial 20 wt % Pt/C (~ 20.4 mg_{Pt} cm^{-2}) ink was prepared by mixing 10 mg of Pt/C with 5 mL aqueous solution (20% IPA, 0.02% Nafion solution). For measurement of oxygen reduction reaction (ORR) activity, linear sweep voltammetry (LSV) was conducted in O_2-saturated 0.1 M $HClO_4$ which was purged with oxygen during measurement. The ORR polarization curves were collected with a sweep rate 5 mV s^{-1} at a rotating speed of 1600 rpm. The long-term durability of $PtNi_{SA\text{-}NPs}$/NDC and commercial Pt/C was performed in O_2-saturated $HClO_4$ solutions by applying cycle voltammetry sweeps between 0.5 and 1.1 V versus RHE at a scan rate of 200 mV s^{-1} over 10,000 cycles. The stability tests were carried out by current versus time (i-t) chronoamperometric response at applied constant voltage at 0.6 V for 50,000 s. For the hydrogen evolution reaction (HER), the glassy carbon (GC diameter = 3 mm) was used as the working electrode, and the Ag/AgCl and graphitic carbon rod were used as reference and counter electrodes, respectively. The LSV curves were obtained at a scan rate of 5 mV s^{-1} in N_2-saturated 0.5 M H_2SO_4. Prior to the HER test, the samples were activated by cycle voltammetry sweeps between 0.2 and − 0.1 V versus RHE at a scan rate of 20 mV s^{-1} for 100 cycles. The HER durability test was performed with 10,000 CV cycles from 0.2 to – 0.1 V (vs. RHE) at a scan rate of 120 mV s^{-1}.

After the durability test, the catalyst on the RDE was removed by placing the RDE in a small vial containing a mixture of ethanol and water with the ratio of 1:1, followed by gentle sonication for 5 min. The obtained suspensions were washed thoroughly with ethanol and water to ensure all the Nafion binder was removed. The catalysts were then dried at 60 °C under vacuum conditions for further analyses.

3. Results and discussion

The overall synthetic strategy is summarized in Fig. 1. Initially, the ZIF-8 crystals were first synthesized, then heated to 900 °C under an argon atmosphere, and then cooled to room temperature to obtain the N-doped carbon framework (NDCF), as reported by Wang et al. [36]. NDCF was thereafter immersed into the solution that contained the target metal ions (Pt^{2+} and Ni^{2+}) to form Pt^{2+}-Ni^{2+}@NDCF with continuous stirring at 80 °C. The high porosity of the NDCF facilitates the effective diffusion and physical adsorption of the metal salts throughout its pore structure. After freeze drying, $PtNi_{SA\text{-}NPs}$/NDCF was formed by pyrolysis at 900 °C for 1 h in an Ar atmosphere. During the pyrolysis process, the metal cations are thermally reduced, leading to the formation of a disordered Pt—Ni alloy. Simultaneously, the acetylacetonate (acac) as a linker between the surface of Pt—Ni alloy and the carbon matrix of NDCF, contributing to the formation of a graphitic carbon layer that encapsulating the alloy NPs. This process ensures the integration of the carbon layer with the alloy NPs, enhancing the material's stability and performance. The same processes were performed to obtain $Pt_{SA\text{-}NPs}$/NDCF and $Ni_{SA\text{-}NPs}$/NDCF with the same metal loading.

Fig. S1 shows the XRD analysis results and TEM images of the ZIF-8 before and after carbonization. The XRD pattern (**Fig. S1**a) shows spectra peaks at 2θ = 7.42°, 10.45°, 12.78°, 14.76°, 16.54° and 18.08°, which correspond to the crystal planes of (011), (002), (112), (022), (013) and (222) of ZIF-8 [47–49]. The TEM image (**Fig. S1**b) confirms that the as-synthesized ZIF-8 crystals are uniform in particle size and present a regular rhombododecahedron shape. As predicted, the resultant NDCF was generated after carbonization process. The XRD diffraction peaks in **Fig. S1**c shows no metallic peaks. A broad peak at 2θ = 25.8 corresponds to graphitic C (002). Furthermore, the TEM image shows that after carbonization, the as-prepared NDCF delivered a highly porous carbon framework (**Fig. S1**d).

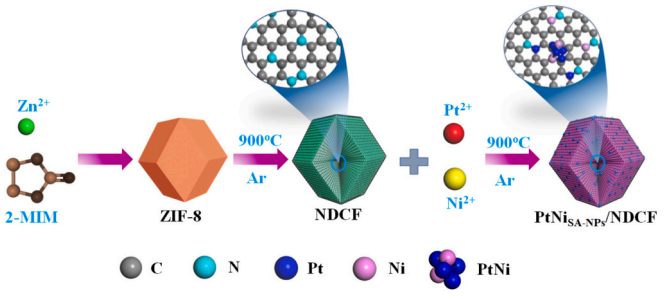


Fig. 1. Schematic diagram describing the synthetic process followed to develop the $PtNi_{SA\text{-}NPs}$/NDCF catalyst.

The FE-SEM image of $PtNi_{SA\text{-}NPs}$/NDCF (Fig. 2a) demonstrates that the porous structure of the rhombododecahedron carbon framework remains stable after the pyrolyzed step of Pt^{2+}-Ni^{2+}@NDCF. As seen from the high-resolution HAADF-STEM images in Fig. 2b, the $PtNi_{SA\text{-}NPs}$/NDCF composite particles have an abundance of uniformly dispersed NPs implanted in the NDCF support with no detectable aggregation. The Pt—Ni alloy NPs are mostly 1–3 nm in size (about 1.9 nm in average). Fig. 2c reveals that the Pt—Ni alloy NPs in $PtNi_{SA\text{-}NPs}$/NDCF are stably fixed within the matrix of the porous NDCF. Inset in Fig. 2c confirms that Pt—Ni alloy NPs in $PtNi_{SA\text{-}NPs}$/NDCF are partially wrapped by graphitic carbon layer and stably fixed in the matrix of the NDCF. This graphitic carbon layer may attribute to prevent the dissolution of Pt—Ni alloy NPs during the stability measurement, resulting the enhancement in durability of $PtNi_{SA\text{-}NPs}$/NDCF catalyst. Furthermore, the porous nature of the NDCF derived from ZIF-8 not only increases the spatial distance to inhibit the aggregation of Pt—Ni alloy NPs, but also provides more accessible reaction interface. Fig. 2d shows the lattice fringes of the Pt—Ni alloy NPs, which is clearly visible with an interplanar spacing of 2.20 Å. Recalling that the interplanar spacing of pure Pt (111) is 2.27 Å and pure Ni (111) is 2.03 Å [50], this indicates that Pt was alloyed with Ni to form Pt—Ni alloy NPs in the $PtNi_{SA\text{-}NPs}$/NDCF catalyst. Meanwhile the enlarged HAADF-STEM in Fig. 2e shows a predominance uniformly dispersed of bright speckled dots (highlighted by the red circles) in this area, which demonstrate that some of the Pt and Ni components are also existed in the form of SA located around the Pt—Ni alloy NPs. The synergistic combination of SAs and alloy NPs for the Pt and Ni elements could have contributed to the improvements in ORR and HER performance [51]. Fig. 2f shows the intensity profile for the Pt and Ni elements within a randomly selected yellow square box in Fig. 2d. The results suggest the existence of Pt—Ni dual SAs and possible formation of Pt—Ni bonds within the matrix of the $PtNi_{SA\text{-}NPs}$/NDCF catalyst. The STEM-EDS mapping (Fig. 2g) and EDS spectrum (**Fig. S2**) of the $PtNi_{SA\text{-}NPs}$/NDCF further confirm the uniform presence of C, N, Pt and Ni elements. The total mass loading of Pt and Ni in $PtNi_{SA\text{-}NPs}$/NDCF was confirmed using ICP-MS technique (**Fig. S3**); Pt was found to be 4.07 wt% and Ni was 1.91 wt%. For comparison, the $Pt_{SA\text{-}NPs}$/NDCF and $Ni_{SA\text{-}NPs}$/NDCF were also prepared with the same metals loading amount. The morphology of the $Pt_{SA\text{-}NPs}$/NDCF and $Ni_{SA\text{-}NPs}$/NDCF catalysts were investigated by SEM and EDX (**Fig. S4** and **S5**, respectively). The $Ni_{SA\text{-}NPs}$/NDCF possessed the regular rhombododecahedron carbon framework structure while the $Pt_{SA\text{-}NPs}$/NDCF structure was damaged and became irregular due to the massive aggregation of Pt particles that were too large and arranged randomly. This may have an outsized effect on the activity and efficiency of $Pt_{SA\text{-}NPs}$/NDCF catalysts.

Fig. 3a shows the XRD patterns of NDCF and $PtNi_{SA\text{-}NPs}$/NDCF catalysts. There is a broaden peak at 2θ of 26.5°, which can be attributed to the specific graphitic features of the carbon material after carbonization [50]. Specially, for the $PtNi_{SA\text{-}NPs}$/NDCF catalyst, there are specific peaks at 2θ of 40.47° and 47.06° that correspond to the (111) and (200) planes of Pt—Ni alloy NPs. Compared to pure Pt (PDF#00–004-0802), these peaks have been shifted to a higher 2θ angle, further suggesting the formation of a Pt—Ni alloy phase structure [52]. Furthermore, a comparison of the Raman spectrum of the $PtNi_{SA\text{-}NPs}$/NDCF and the NDCF in **Fig. S6** clearly shows the graphitic state of the carbon framework, as evidenced by the presence of D-band and G-band peaks at 1350 and 1575 cm^{-1}, respectively. The D-band represents the structural defects caused by heteroatom doping, while the G-band shows the large

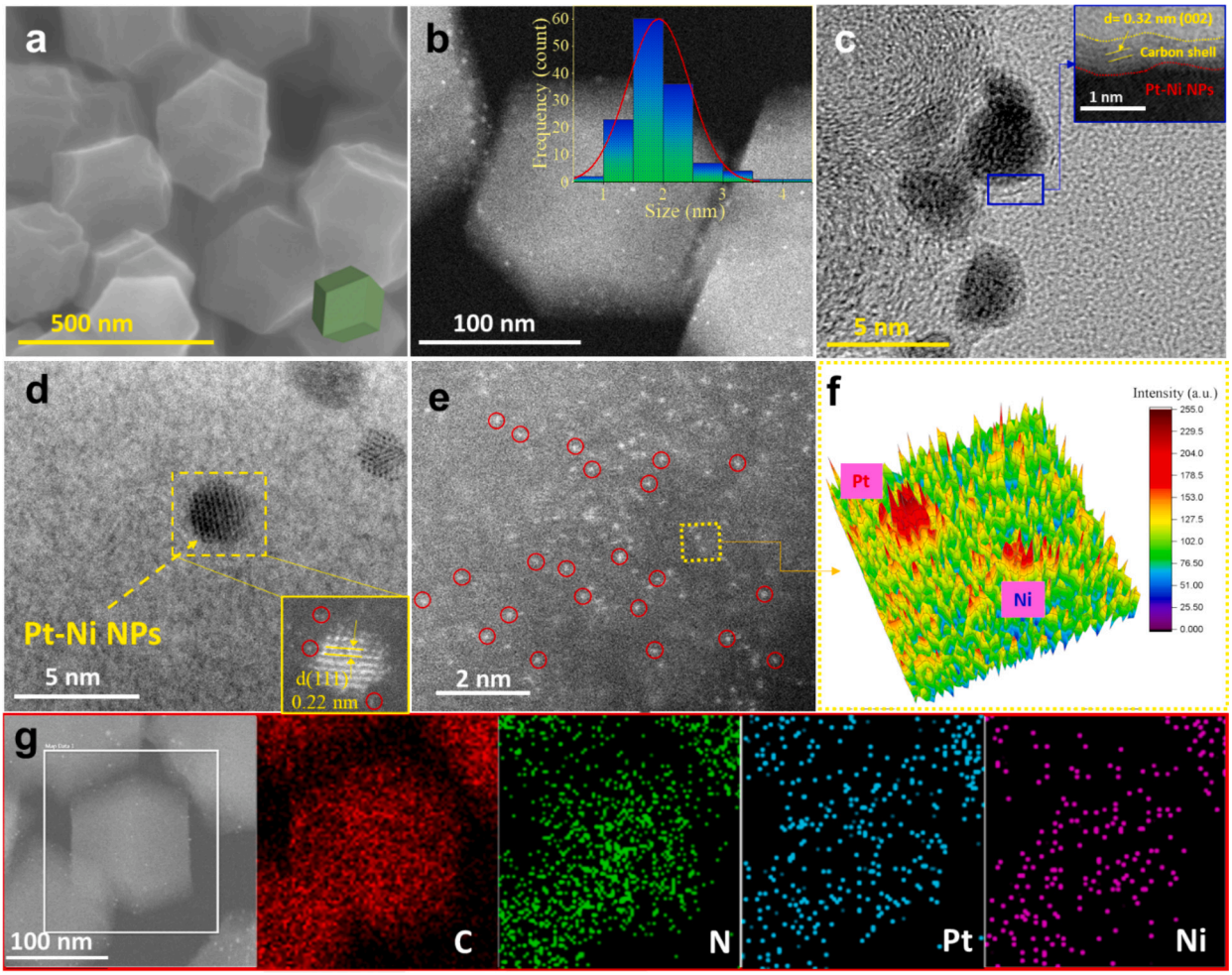


Fig. 2. (a) FE-SEM image of $PtNi_{SA\text{-}NPs}$/NDCF catalyst. (b) low HAADF-STEM images of $PtNi_{SA\text{-}NPs}$/NDCF catalyst, the inset is the size distribution of Pt—Ni alloy NPs. (c) High-resolution HAADF-STEM images of $PtNi_{SA\text{-}NPs}$/NDCF catalyst, the inset show the carbon shell thickness is around 1 nm. (d) CS-corrected TEM image of $PtNi_{SA\text{-}NPs}$/NDCF catalyst at an area containing Pt—Ni NPs along with the crystalline feature of the area indicated by yellow box. (e) HAADF-STEM image of $PtNi_{SA\text{-}NPs}$/NDCF at an area without NPs. (f) The intensity profile obtained at site the yellow box in (e). (g) HAADF-STEM image and corresponding EDS maps of $PtNi_{SA\text{-}NPs}$/NDCF showing the uniform dispersion of C (red), N (green), Pt (cyan) and Ni (pink).

conjugated carbon skeleton formed by the sp^2 hybridization of graphene [44]. The D-band and G-band intensities (I_D/I_G), which are often used to determine the level of graphitization and number of defects of the carbon support. There is an increase in I_D/I_G in $PtNi_{SA\text{-}NPs}$/NDCF (2.71) as compared to that of NDCF (2.51), implying that the introduction of Pt and Ni metal atoms into the carbon framework matrix generates more defects and vacancies [12,53]. Furthermore, the introduction of heteroatom (such as N, Pt or Ni) into the matrix of graphitic carbon has been demonstrated to cause the electronic modulation to provide a desirable electronic structure and enhance electrocatalytic activity toward ORR and HER [54]. Notably, the nitrogen adsorption-desorption analysis in Fig. 3b shows that all samples displayed a hysteresis loop and relative pressure that correspond to 1 ($P/P_0 = 1$), indicating that the as-synthesized catalysts have both mesopore and micropore properties [47,55]. Due to Pt and Ni doping into the NDCF support, the $PtNi_{SA\text{-}NPs}$/NDCF possesses a beneficial specific surface area of 1135 $m^2\ g^{-1}$, which higher than that of NDCF (823 $m^2\ g^{-1}$). The ultrahigh specific surface area of $PtNi_{SA\text{-}NPs}$/NDCF can effectively prevent metal agglomeration and improve the atomic content in the final catalyst to produce more active sites for electrocatalytic reactions, such as ORR and HER [56–58].

We performed an XPS analysis to gain further insight into the chemical composition and valence state of the synthesized catalysts. The full survey spectra of the $PtNi_{SA\text{-}NPs}$/NDCF, $Pt_{SA\text{-}NPs}$/NDCF and $Ni_{SA\text{-}NPs}$/NDCF is shown **Fig. S7**. A high-resolution C 1 s spectrum of the $PtNi_{SA\text{-}NPs}$/NDCF (Fig. 3c) reveals five dominant peaks at 284, 285.1, 286.4 eV, 289.1, and 287.8 eV, corresponding to sp^2 carbon bonding (sp^2 C-C/C-H), sp^3 carbon bonding (sp^3 C—C), C-O/C-N bonding, O-C=O bonding, and C=O/C-N bonding, respectively [18,59–62]. Notably, the sp^2 carbon species, identified as graphitic carbon, exhibits the highest ratio at 89.1%. This graphitic carbon structure is highly stable and resistant to oxygen oxidation [54], which may be beneficial for protecting the Pt—Ni alloy nanoparticles encapsulated within it. A light peak at 290.9 eV is attributed to the π-π* interaction caused by the vibration of aromatic rings [63]. The high-resolution XPS spectrum of the N 1 s (Fig. 3d) reveals the coexistence of pyrrolic-N (399.9 eV, 7.21%), oxidized-N (402.9 eV, 9.63%), graphitic-N (400.3 eV, 25.69%), and pyridinic-N (397.8 eV, 45.11%). Interestingly, a high proportion of Pt—N or Ni—N bonding is also observed (398.6 eV, 12.35%) [17], similar to the formation of the Fe—N bonding observed on Fe-N_x/C catalysts [58,64]. In another regard, a prominent pyridinic-N peak can be expected to serve as an anchor point for the stabilizing Pt-N_x and Ni-N_x coordination in the NDCF matrix, and significantly reduce the localization of electrons around the Pt and Ni center, thereby promoting ORR and HER [65]. The relatively high proportion of graphitic N is stable and beneficial to rapid electron transfer, enhancing the durability and electrocatalytic activity of these catalyst materials [37]. As shown in Fig. 3e, the Pt 4f spectrum of the $PtNi_{SA\text{-}NPs}$/NDCF displays two doublet peaks that correspond to the Pt metal state peaks from the core Pt—Ni alloy with Pt^0 4f binding

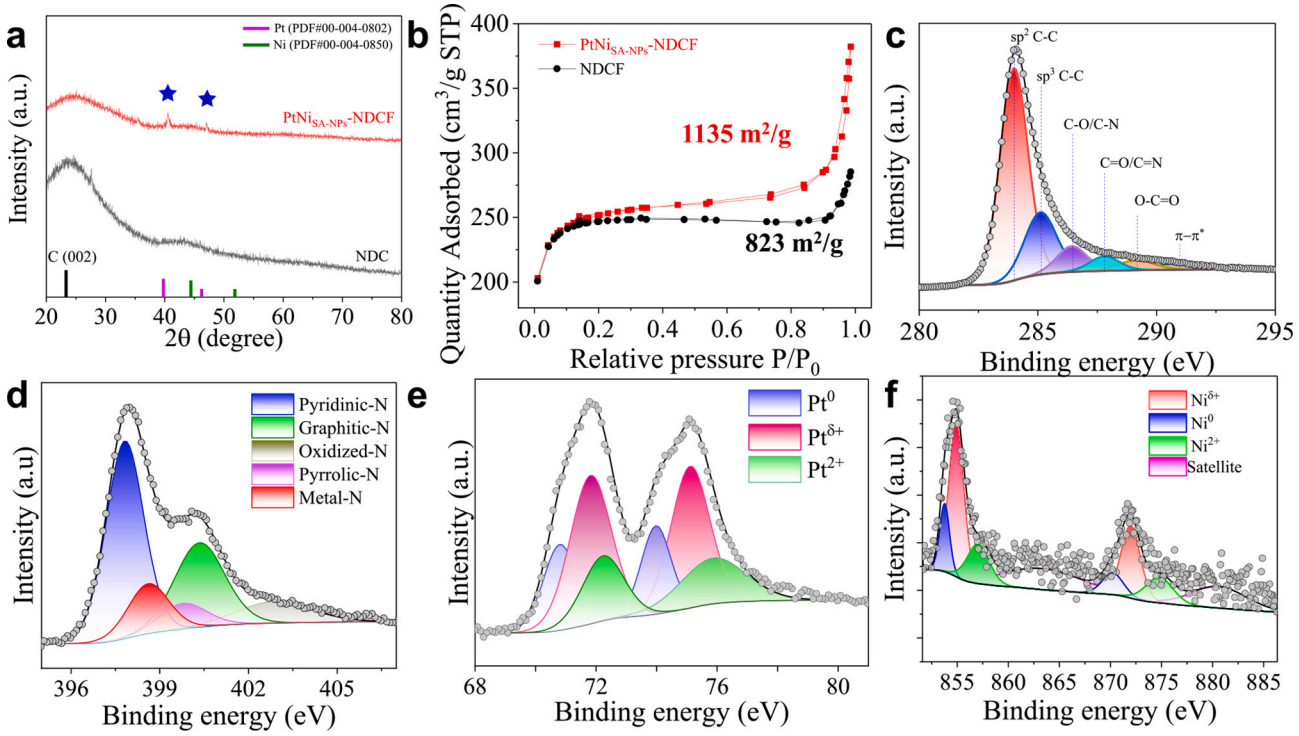


Fig. 3. (a) XRD spectra, (b) Nitrogen adsorption-desorption isotherms of PtNi$_{SA-NPs}$/NDCF and NDCF. High-resolution XPS spectra of (c) C 1 s, (d) N 1 s, (e) Pt 4f, and (f) Ni 2p for PtNi$_{SA-NPs}$/NDCF.

energies at 70.80 and 73.98 eV (24.0%), oxidized Pt state peaks from the surface of the Pt—Ni alloy with Pt^{2+} binding energies at 72.23 and 75.87 eV (24.9%) and major oxidation state $Pt^{\delta+}$ peaks (71.82 and 85.11 eV, 54.1%) caused by the interaction of isolated Pt SA and neighbor pyridinic-N to form a stable Pt-N_x coordination active site [66]. This result is consistent with our HAADF-STEM analysis and confirms the coexistence of Pt SA ($Pt^{\delta+}$) and metallic Pt in the Pt—Ni alloy (Pt^0 core and Pt^{2+} surface). Comparing this with the high-resolution XPS spectra of the Pt$_{SA-NPs}$/NDCF in **Fig. S8**a, a positive shift of binding energy is adverted for the Pt 4f doublet peaks in PtNi$_{SA-NPs}$/NDCF,

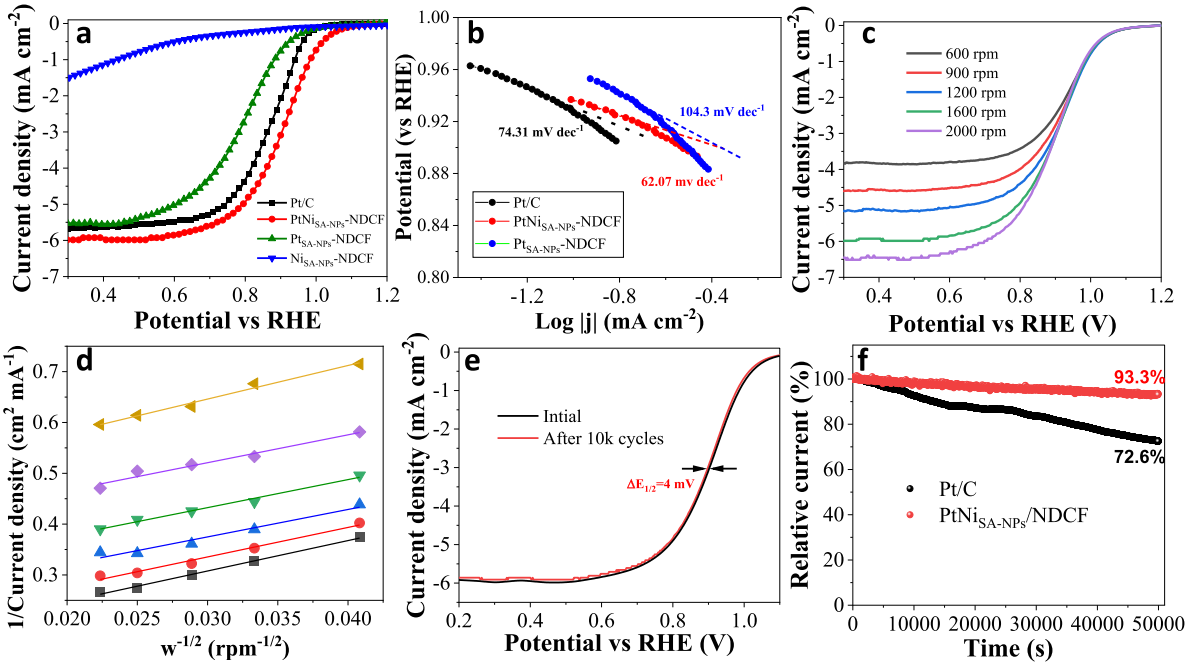


Fig. 4. (a) LSV responses, (b) Tafel slope of different catalyst materials in O_2-saturated 0.1 M $HClO_4$ solution, (c) ORR polarization curves of PtNi$_{SA-NPs}$/NDCF in O_2-saturated 0.1 M $HClO_4$ solution with various rotation rates at a scan speed of 5 mV s^{-1}, (d) Koutecky-Levich plots of PtNi$_{SA-NPs}$/NDCF collected from the ORR polarization curves, (e) Cycling stability of PtNi$_{SA-NPs}$/NDCF over 10, 000 cycles, (f) Long-term i-*t*-test performed at the constant overpotential of 0.6 V (vs RHE) of PtNi$_{SA-NPs}$/NDCF and Pt/C in 0.1 M $HClO_4$.

suggesting a robust electronic interaction between the Pt and Ni atoms. The electrons may have transferred from Ni to Pt due to its higher electronegativity. This is further supported by the negative shift in the $Pt^{\square+}$ peak of $PtNi_{SA\text{-}NPs}$/NDCF compared with $Pt_{SA\text{-}NPs}$/NDCF, confirming the synergistic effect between the Pt—Ni alloy NPs and Pt, Ni SAs [67]. Meanwhile, the Ni 2p XPS spectrum (Fig. 3f) shows the coexistence of an Ni metal state within the core of the Pt—Ni alloy NPs with Ni^0 2p binding energies at 853.77 eV and 870.24 eV (12.11%), the oxidation states of Ni SA triggered by the Ni-N_x interaction with the $Ni^{\delta+}$ binding energies at 854.92 eV and 871.91 eV (40.12%), the oxidized state Ni^{2+} from the surface of the alloy NPs with binding energies at 857.05 and 874.80 (17.04%) and a minor satellite characteristic at 863.35 eV and 880.62 eV (30.74%). Interestingly, the Ni 2p binding energies in the $Ni_{SA\text{-}NPs}$/NDCF (**Fig. S8**b) are displayed a negative shift than the $PtNi_{SA\text{-}NPs}$/NDCF, suggesting some surface modification of the electronic structure after anchoring with the Pt atoms [68].

In light of the exciting physicochemical properties shown by the $PtNi_{SA\text{-}NPs}$/NDCF, the ORR performance of the synthesized catalysts was assessed in acidic media using a typical three-electrode system at room temperature (Fig. 4). As a comparator, a commercial 20 wt% Pt/C catalyst was also tested. The LSV polarization curves of the different materials in the O_2-saturated 0.1 M $HClO_4$ electrolyte at a rotation speed of 1600 rpm are shown in Fig. 4a. The ORR activity trend can be expressed in the following order: $PtNi_{SA\text{-}NPs}$/NDCF > Pt/C > $Pt_{SA\text{-}NPs}$/NDCF > $Ni_{SA\text{-}NPs}$/NDCF. Compared to the $Pt_{SA\text{-}NPs}$/NDCF, the $Ni_{SA\text{-}NPs}$/NDCF shows lower ORR performance with a half-wave potential ($E_{1/2}$) of 0.51 V vs the reversible hydrogen electrode (RHE), suggesting the Ni-metal catalyst are almost inert to the ORR process. The $PtNi_{SA\text{-}NPs}$/NDCF exhibits significant ORR activity, which delivers an onset potential of +1.01 V vs RHE and half-wave potential of +0.91 V vs RHE, which is superior to $Pt_{SA\text{-}NPs}$/NDCF, $Ni_{SA\text{-}NPs}$/NDCF, and even better than Pt/C, confirming the beneficial role of the Pt—Ni synergistic effect. The catalytic activity of $PtNi_{SA\text{-}NPs}$/NDCF is also superior to many ORR electrocatalysts reported elsewhere (**Table S1**).

A Tafel slope was performed to evaluate the ORR kinetic on the surface of the catalyst. As seen in Fig. 4b, the Tafel slope of the $PtNi_{SA\text{-}NPs}$/NDCF is approximately 62.07 mV dec^{-1}, lower than that of Pt/C (74.31 mV dec^{-1}) and $Pt_{SA\text{-}NPs}$/NDCF (104.3 mV dec^{-1}), demonstrating that $PtNi_{SA\text{-}NPs}$/NDCF has a faster ORR kinetic than both. To explore the catalytic selectivity toward ORR, the LSV curves of the $PtNi_{SA\text{-}NPs}$/NDCF was determined under diverse speeds between 600 and 2000 rpm a means of estimating number of electron transfer (*n*) value and main ORR pathway (Fig. 4c) [69]. We determined that the onset potential of remains constant and the current density gradually increases while rotation speed increases. As shown in Fig. 4d, the fitting plots at different potentials display a good liner relationship, suggesting a first-order kinetic of the ORR process. Applying the *Koutecky-Levich (K-L)* equation, the *n* value of the $PtNi_{SA\text{-}NPs}$/NDCF can be estimated as 3.91 in the surveyed potential range of 0.2 to 0.7 V_{RHE}, indicating that its ORR process is highly closed to the four-electron transfer reaction pathway, where the oxygen is reduced into water ($O_2 + 2H_2O + 4e^- \rightarrow 4OH^-$) [70,71].

The stability of the catalysts was evaluated using accelerating durability tests (ADT) with cycling potential between 0.5 V and 1.0 V in O_2-saturated $HClO_4$ electrolyte (Fig. 4e). After 10,000 cycles, the half-wave potential of the $PtNi_{SA\text{-}NPs}$/NDCF showed only a − 4 mV negative shift, while a − 48 mV shift was observed for Pt/C (**Fig. S9**). The stability tests were performed using a current vs time (i-t) chronoamperometric response at an applied bias voltage of 0.6 V_{RHE} for 50,000 s. As shown in Fig. 4f, the normalized current loss of $PtNi_{SA\text{-}NPs}$/NDCF was only 6.7%, much smaller than that of commercial Pt/C (27.4%). Additionally, due to the low specific surface area and nonporous carbon support, the Pt/C catalyst generally suffers severe degradation during the ADT due to the Ostwald ripening, the migration and agglomeration of Pt NPs, and carbon corrosion [72]. This result highlights the improvement in the stability of the $PtNi_{SA\text{-}NPs}$/NDCF catalyst compared to the commercial Pt/C catalyst.

The HER properties of the $PtNi_{SA\text{-}NPs}$/NDCF, $Pt_{SA\text{-}NPs}$/NDCF, $Ni_{SA\text{-}NPs}$/NDCF, NDCF, and commercial 20% Pt/C catalysts were investigated in N_2-saturated 0.5 M H_2SO_4 electrolytes at ambient temperature. As displayed in Fig. 5a, the $PtNi_{SA\text{-}NPs}$/NDCF catalyst showed outstanding catalytic performance for HER, substantially higher than that of a commercial Pt/C, $Pt_{SA\text{-}NPs}$/NDCF, $Ni_{SA\text{-}NPs}$/NDCF, and NDCF. At a polarization current density of −10 mA cm^{-2}, the record overpotential for $PtNi_{SA\text{-}NPs}$/NDCF requires 24.7 mV (vs RHE), which is more positive than those obtained by Pt/C (43.9 mV), $Pt_{SA\text{-}NPs}$/NDCF (66.0 mV), and significant improvement over $Ni_{SA\text{-}NPs}$/NDCF (195 mV). The NDCF was nearly inert toward HER, demonstrating that HER only occurred on the metal's atom active sites. A comparison between the $PtNi_{SA\text{-}NPs}$/NDCF and others recently reported catalysts further demonstrated the former's superior HER performance in acidic electrolyte (**Table S2**). As shown in Fig. 5b, at the current density reaches −50 mA cm^{-2}, only a smaller ~44 mV was required overpotential, compared with those of Pt/C (~75.7 mV), $Pt_{SA\text{-}NPs}$/NDCF (~105.8 mV) and $Ni_{SA\text{-}NPs}$/NDCF (~303 mV).

The Tafel slopes of these synthesized catalyst were examined to determine the intrinsic kinetic process toward HER. The results obtained are shown in Fig. 5c. As observed, the Tafel slope of the $PtNi_{SA\text{-}NPs}$/NDCF catalyst possesses approximately 16.2 mV dec^{-1}, which is remarkably lower than those of the Pt/C (~30.8 mV dec^{-1}), $Pt_{SA\text{-}NPs}$/NDCF (31.6 mV dec^{-1}) and $Ni_{SA\text{-}NPs}$/NDCF (104 mV dec^{-1}). According to classical theory, three principal steps are involved in the reaction that transforms $2H^+$ to H_2; these are commonly referred to as the Volmer (1) step, the Heyrovsky (2) step, and the Tafel (3) step [73].

$$\text{Volmer step}: H_2O + e^- \rightarrow H^* + OH^- \sim 120\ \text{mV dec}^{-1} \quad (1)$$

$$\text{Heyrovsky step}: H^* + H_2O + e^- \rightarrow H_2 + OH^- \sim 40\ \text{mV dec}^{-1} \quad (2)$$

$$\text{Tafel}: H^* \rightarrow 2\,H_2 \sim 30\ \text{mV dec}^{-1} \quad (3)$$

Combinations of steps (1) and (2) or (1) and (3), i.e., Volmer–Heyrovsky or Volmer–Tafel steps, can lead to the production of molecular H_2. The Tafel slope we observed suggests that the HER process over $PtNi_{SA\text{-}NPs}$/NDCF catalyst follows the Volmer−Tafel mechanism pathway, in which the Tafel step is the rate-limiting step at low overpotentials [74].

To further explore the intrinsic activity, the LSV polarization curve of the $PtNi_{SA\text{-}NPs}$/NDCF and commercial Pt/C was normalized by Pt loading on the electrode (Fig. 5d) to calculate the mass activity. As observed in Fig. 5e, at an overpotential of 25 mV and 40 mV, the recorded mass activity of $PtNi_{SA\text{-}NPs}$/NDCF were 1.6 and 6.1 A mg_{Pt}^{-1}, which are respectively 13- times and 18.5- times higher than that of the commercial Pt/C. These results indicate that the $PtNi_{SA\text{-}NPs}$/NDCF has a high abundance of active site from the Pt and Ni SAs and the Pt—Ni alloy NPs that boost HER performance. Moreover, the charge-transfer efficiency of the synthesized catalysts was determined by EIS. The Nyquist diagram (Fig. 5f) of the $PtNi_{SA\text{-}NPs}$/NDCF displays the smallest semicircle and the most horizontal Warburg portion when compared to the $Pt_{SA\text{-}NPs}$/NDCF, $Ni_{SA\text{-}NPs}$/NDCF and Pt/C, demonstrating the superior mass diffusion process and the charge transfer at the $PtNi_{SA\text{-}NPs}$/NDCF electrode-electrolyte interface, and reflecting a rapid reaction rate [75]. Fig. 5g presents the equivalent model of the EIS test. The catalyst durability of the $PtNi_{SA\text{-}NPs}$/NDCF was investigated through an accelerated durability test (ADT) for 10, 000 CV cycles under N_2-saturated 0.5 M H_2SO_4 electrolyte [76]. As shown in Fig. 5h, the $PtNi_{SA\text{-}NPs}$/NDCF does show a negligible negative shift (a mere 6 mV) at a current density of 10 mA cm^{-2}, meanwhile the commercial Pt/C exhibited decay of 14 mV (Fig. 5i), highlighting the remarkable stability of the $PtNi_{SA\text{-}NPs}$/NDCF.

In order to determine whether $PtNi_{SA\text{-}NPs}$/NDCF catalyst's structural characteristics changed significantly after the long-term durability test, FESEM, TEM, XPS, and Raman analyses were performed after 10,000 CV

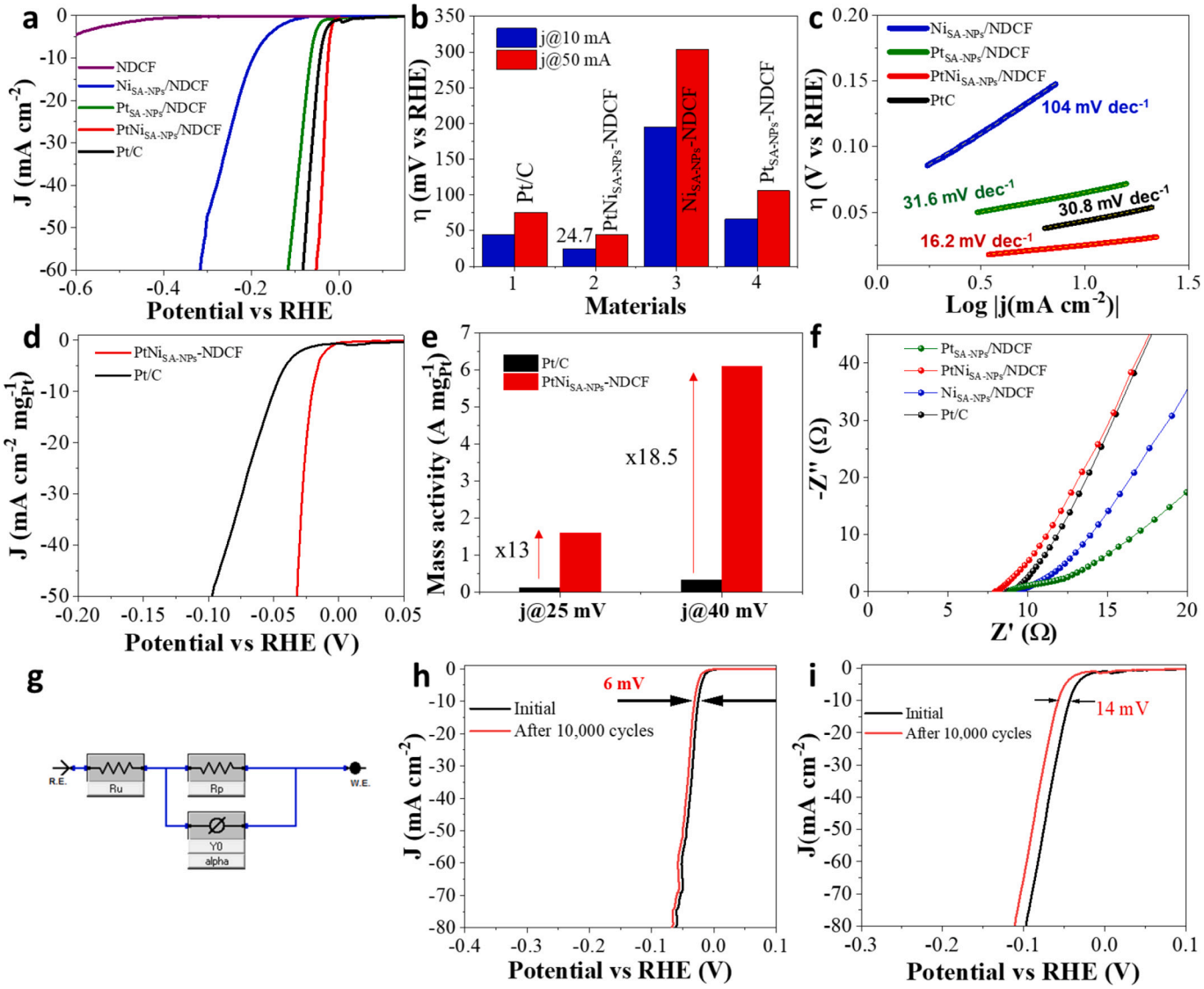


Fig. 5. HER polarization curves of $PtNi_{SA\text{-}NPs}$/NDCF, $Pt_{SA\text{-}NPs}$/NDCF, $Ni_{SA\text{-}NPs}$/NDCF, NDCF, and 20 wt% Pt/C in 0.5 M H_2SO_4 solution at a scan rate of 5 mV s^{-1}, (b) the corresponding overpotential of these catalyst materials @j = 10/50 mA cm^{-2}, (c) Tafel slopes of different catalyst materials, (d) LSV curves of $PtNi_{SA\text{-}NPs}$/NDCF and Pt/C normalized by Pt loading on the electrodes, (e) Mass activity of $PtNi_{SA\text{-}NPs}$/NDCF and Pt/C at 25 and 40 mV. (f) EIS measurement of different synthesized $PtNi_{SA\text{-}NPs}$/NDCF, $Pt_{SA\text{-}NPs}$/NDCF and $Ni_{SA\text{-}NPs}$/NDCF at OCP value, (g) the equivalent circuit model for the EIS test. LSV polarization curves of $PtNi_{SA\text{-}NPs}$/NDCF (h) and commercial Pt/C (i) before and after 10, 000 CV cycles.

cycles (Fig. 6). The FESEM results indicate that the $PtNi_{SA\text{-}NPs}$/NDCF after 10, 000 CV cycles maintained its initial porosity and rhombododecahedron nanoarchitecture, similar to the primary sample (Fig. 6a). The mean size of the Pt—Ni alloy NPs in $PtNi_{SA\text{-}NPs}$/NDCF only slightly increased by 8% (1.95 nm in the initial sample and 2.12 in the post-durability test sample), as seen in Fig. 6b. We also recorded the chemical state and composition through XPS analysis, with the results displayed in Fig. 6c-g. The binding energies of C 1 s, N 1 s, Pt 4f and Ni 2p retained their initial characteristics, with little modification caused by the ionization or electron changes during the 10, 000 CV cycles. Further, it has been previously reported that the chemical-adsorption oxygen on the catalyst that is exposed to the air is not stable in the ORR reaction [77]. The XPS spectrum O 1 s in Fig. 6g does not show any detectable metal-oxide peak change before and after cycling. Thus, we conclude that the $PtNi_{SA\text{-}NPs}$/NDCF possesses a remarkable structural and chemical stability even after the long-term durability test in acidic medium. It is generally believed that the physical encapsulation of carbon support shell would could contribute to the superior durability of the catalyst [78,79]. We further investigated the stability of the N-doped carbon framework by Raman spectroscopy and compared it with carbon in Pt/C (Fig. 6h and i, respectively). The degree of graphitization of the $PtNi_{SA\text{-}NPs}$/NDCF at initial sample is $I_D/I_G = 2.71$, which slightly decreased to $I_D/I_G = 2.68$ after ADT. In contrast, there was a significant decrease in the commercial Pt/C after ADT (from $I_D/I_G = 1.56$ to 1.37). The reason for the anticorrosion effect in PtNiSA-NPs/NDCF could be assumed to the carbon shell that partially protect the Pt—Ni from dissolution and agglomeration, while enriching of pyridinic-N coordination, and with this as an anchoring point, effectively stabilizing SAs (Pt, Ni) during the electrochemical reactions.

4. Conclusions

In sum, we have successfully produced a unique catalyst with simultaneously anchored Pt and Ni dual SAs and Pt—Ni alloy NPs of a uniform particle size implanted in NDCF. The high specific surface area with abundant N-doping allows the NDCF support to provide a high density of SAs (Pt, Ni) active sites and for a uniform distribution of Pt—Ni alloy NPs. The synergistic effect between the SAs (Pt, Ni) and the

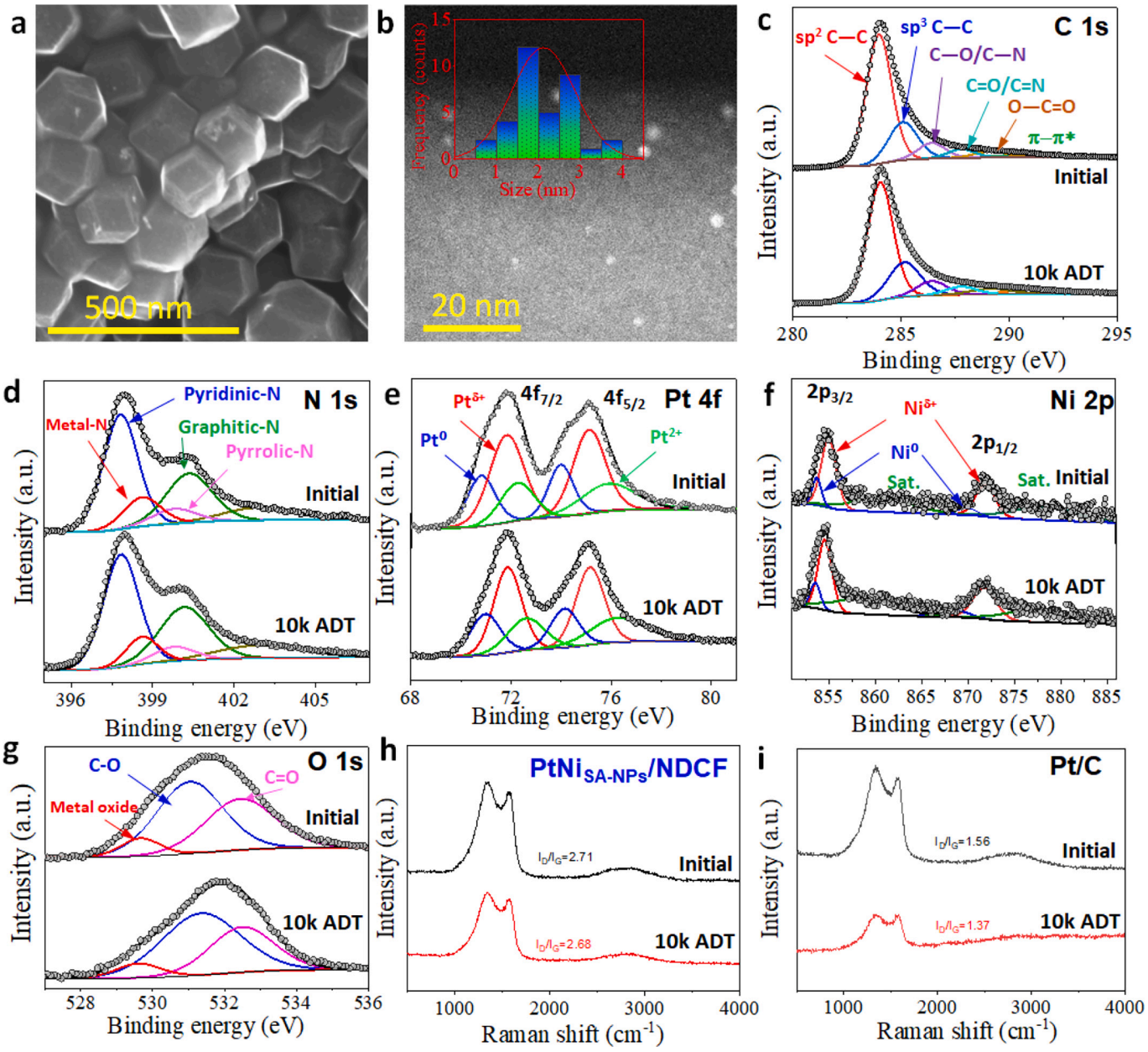


Fig. 6. (a) FE-SEM and (b) HAADF-STEM images of $PtNi_{SA\text{-}NPs}$/NDCF after 10,000 CV cycles stability test. High-resolution XPS spectra of (c) C 1 s, (d) N 1 s, (e) Pt 4f, (f) Ni 2p and (g) O 1 s for $PtNi_{SA\text{-}NPs}$/NDCF before and after accelerated durability test. Raman spectrum of (h) $PtNi_{SA\text{-}NPs}$/NDCF and (i) Pt/C at initial and post-ADT.

Pt—Ni alloy NPs in the $PtNi_{SA\text{-}NPs}$/NDCF electrocatalyst results in exceptional bifunctional performance for both ORR and HER. This is evidenced by an elevated half-wave potential for ORR (0.91 V) and a reduced overpotential at the current density of 10 mA cm^{-2} for HER (24.7 mV). Moreover, relatively high durability of the $PtNi_{SA\text{-}NPs}$/NDCF electrocatalyst could be attributed to the high proportion of pyridinic-N that stabilizing Pt, Ni atoms into the carbon framework matrix and the physical encapsulation of carbon shell that protect Pt—Ni alloy NPs from dissolution and agglomeration. Our findings suggest that this ultralow Pt-based catalyst has potential as a next generation electrocatalytic material suitable for incorporation into for fuel cells and hydrogen production.

CRediT authorship contribution statement

Thanh Duc Le: Conceptualization, Data curation, Formal analysis, Investigation, Methodology, Writing – original draft. **Dong-Seog Kim:** Investigation, Software. **Geun-Jae Oh:** Formal analysis. **Gi-Seung Shin:** Formal analysis. **Tuong Van Tran:** Software. **Yeon-Tae Yu:** Funding acquisition, Project administration, Supervision, Visualization, Writing – review & editing. **Byung-Guk Ahn:** Writing – review & editing.

Declaration of competing interest

The authors declare no competing financial interest.

Data availability

Data will be made available on request.

Acknowledgment

This research was supported by the National Research Foundation (NRF) of Korea Grant funded by the Korean Government (MSIP) (NRF-

2021R1A2C2008447), the BK21-FOUR program of the MOE and NRF of Korea, and the Regional Innovation Strategy (RIS)" through the National Research Foundation of Korea(NRF) funded by the Ministry of Education(MOE)(2023RIS-008).

Appendix A. Supplementary data

Supplementary data to this article can be found online at https://doi.org/10.1016/j.susmat.2024.e01068.

References

[1] Z. Song, Y.-N. Zhu, H. Liu, M.N. Banis, L. Zhang, J. Li, K. Doyle-Davis, R. Li, T.-K. Sham, L. Yang, A. Young, G.A. Botton, L.-M. Liu, X. Sun, Engineering the low coordinated Pt single atom to achieve the superior Electrocatalytic performance toward oxygen reduction, Small 16 (2020), https://doi.org/10.1002/smll.202003096, 2003096.

[2] W. Li, Y. Xiong, Z. Wang, M. Bao, J. Liu, D. He, S. Mu, Seed-mediated synthesis of large-diameter ternary TePtCo nanotubes for enhanced oxygen reduction reaction, Appl. Catal. B Environ. 231 (2018) 277–282, https://doi.org/10.1016/j.apcatb.2018.03.022.

[3] J. Guo, Y. Li, Y. Cheng, L. Dai, Z. Xiang, Highly efficient oxygen reduction reaction electrocatalysts synthesized under nanospace confinement of metal–organic framework, ACS Nano 11 (2017) 8379–8386, https://doi.org/10.1021/acsnano.7b03807.

[4] P. Huang, H. Li, X. Huang, D. Chen, Multiheteroatom-doped porous carbon catalyst for oxygen reduction reaction prepared using 3D network of ZIF-8/polymeric nanofiber as a facile-doping template, ACS Appl. Mater. Interfaces 9 (2017) 21083–21088, https://doi.org/10.1021/acsami.7b06427.

[5] D.S. He, D. He, J. Wang, Y. Lin, P. Yin, X. Hong, Y. Wu, Y. Li, Ultrathin icosahedral Pt-enriched Nanocage with excellent oxygen reduction reaction activity, J. Am. Chem. Soc. 138 (2016) 1494–1497, https://doi.org/10.1021/jacs.5b12530.

[6] Z. Wang, H. Jin, T. Meng, K. Liao, W. Meng, J. Yang, D. He, Y. Xiong, S. Mu, Fe, Cu-Coordinated ZIF-Derived Carbon Framework for Efficient Oxygen Reduction Reaction and Zinc–Air Batteries, Adv. Funct. Mater. 28 (2018), https://doi.org/10.1002/adfm.201802596, 1802596.

[7] M. Luo, S. Guo, Strain-controlled electrocatalysis on multimetallic nanomaterials, Nat. Rev. Mater. 2 (2017) 17059, https://doi.org/10.1038/natrevmats.2017.59.

[8] Z. Zhao, C. Chen, Z. Liu, J. Huang, M. Wu, H. Liu, Y. Li, Y. Huang, Pt-based nanocrystal for Electrocatalytic oxygen reduction, Adv. Mater. 31 (2019), https://doi.org/10.1002/adma.201808115, 1808115.

[9] X. Tian, X. Zhao, Y.-Q. Su, L. Wang, H. Wang, D. Dang, B. Chi, H. Liu, E.J. M. Hensen, X.W. David Lou, B.Y. Xia, Engineering bunched Pt-Ni alloy nanocages for efficient oxygen reduction in practical fuel cells, Science 366 (80) (2019) 850–856, https://doi.org/10.1126/science.aaw7493.

[10] X. Cui, W. Li, P. Ryabchuk, K. Junge, M. Beller, Bridging homogeneous and heterogeneous catalysis by heterogeneous single-metal-site catalysts, Nat. Catal. 1 (2018) 385–397, https://doi.org/10.1038/s41929-018-0090-9.

[11] L. Liu, A. Corma, Metal catalysts for heterogeneous catalysis: from single atoms to nanoclusters and nanoparticles, Chem. Rev. 118 (2018) 4981–5079, https://doi.org/10.1021/acs.chemrev.7b00776.

[12] T. Zhang, X. Han, H. Yang, A. Han, E. Hu, Y. Li, X. Yang, L. Wang, J. Liu, B. Liu, Atomically dispersed nickel(I) on an alloy-encapsulated nitrogen-doped carbon nanotube Array for high-performance electrochemical CO2 reduction reaction, Angew. Chem. Int. Ed. 59 (2020) 12055–12061, https://doi.org/10.1002/anie.202002984.

[13] S. Liang, C. Hao, Y. Shi, The power of single-atom catalysis, Chem. Cat. Chem. 7 (2015) 2559–2567, https://doi.org/10.1002/cctc.201500363.

[14] W. Zhang, W. Zheng, Single atom excels as the smallest functional material, Adv. Funct. Mater. 26 (2016) 2988–2993, https://doi.org/10.1002/adfm.201600240.

[15] S. Yang, J. Kim, Y.J. Tak, A. Soon, H. Lee, Single-atom catalyst of platinum supported on titanium nitride for selective electrochemical reactions, Angew. Chem. Int. Ed. 55 (2016) 2058–2062, https://doi.org/10.1002/anie.201509241.

[16] C.H. Choi, M. Kim, H.C. Kwon, S.J. Cho, S. Yun, H.-T. Kim, K.J.J. Mayrhofer, H. Kim, M. Choi, Tuning selectivity of electrochemical reactions by atomically dispersed platinum catalyst, Nat. Commun. 7 (2016) 10922, https://doi.org/10.1038/ncomms10922.

[17] J. Liu, M. Jiao, L. Lu, H.M. Barkholtz, Y. Li, Y. Wang, L. Jiang, Z. Wu, D. Liu, L. Zhuang, C. Ma, J. Zeng, B. Zhang, D. Su, P. Song, W. Xing, W. Xu, Y. Wang, Z. Jiang, G. Sun, High performance platinum single atom electrocatalyst for oxygen reduction reaction, Nat. Commun. 8 (2017) 15938, https://doi.org/10.1038/ncomms15938.

[18] P.S. Goohpattader, N. Dwivedi, E. Rismani-Yazdi, N. Satyanarayana, R.J. Yeo, S. Kundu, C.S. Bhatia, Probing the role of C+ ion energy, thickness and graded structure on the functional and microstructural characteristics of ultrathin carbon films (<2nm), Tribol. Int. 81 (2015) 73–88, https://doi.org/10.1016/j.triboint.2014.08.001.

[19] B. Lu, Q. Liu, F. Nichols, R. Mercado, D. Morris, N. Li, P. Zhang, P. Gao, Y. Ping, S. Chen, Oxygen reduction reaction catalyzed by carbon-supported platinum few-atom clusters: significant enhancement by doping of atomic cobalt, Research 2020 (2020), https://doi.org/10.34133/2020/9167829, 9167829.

[20] L. Zhang, J.M.T.A. Fischer, Y. Jia, X. Yan, W. Xu, X. Wang, J. Chen, D. Yang, H. Liu, L. Zhuang, M. Hankel, D.J. Searles, K. Huang, S. Feng, C.L. Brown, X. Yao, Coordination of atomic co–Pt coupling species at carbon defects as active sites for oxygen reduction reaction, J. Am. Chem. Soc. 140 (2018) 10757–10763, https://doi.org/10.1021/jacs.8b04647.

[21] R. Gao, J. Wang, Z.-F. Huang, R. Zhang, W. Wang, L. Pan, J. Zhang, W. Zhu, X. Zhang, C. Shi, J. Lim, J.-J. Zou, Pt/Fe2O3 with Pt–Fe pair sites as a catalyst for oxygen reduction with ultralow Pt loading, Nat. Energy 6 (2021) 614–623, https://doi.org/10.1038/s41560-021-00826-5.

[22] M. Busch, E. Ahlberg, I. Panas, Validation of binuclear descriptor for mixed transition metal oxide supported electrocatalytic water oxidation, Catal. Today 202 (2013) 114–119, https://doi.org/10.1016/j.cattod.2012.04.060.

[23] M. Busch, N.B. Halck, U.I. Kramm, S. Siahrostami, P. Krtil, J. Rossmeisl, Beyond the top of the volcano? – a unified approach to electrocatalytic oxygen reduction and oxygen evolution, Nano Energy 29 (2016) 126–135, https://doi.org/10.1016/j.nanoen.2016.04.011.

[24] N. Alonso-Vante, Parameters affecting the fuel cell reactions on platinum bimetallic nanostructures, Electrochem. Energy Rev. 6 (2023) 3, https://doi.org/10.1007/s41918-022-00145-7.

[25] C. Cui, L. Gan, M. Heggen, S. Rudi, P. Strasser, Compositional segregation in shaped Pt alloy nanoparticles and their structural behaviour during electrocatalysis, Nat. Mater. 12 (2013) 765–771, https://doi.org/10.1038/nmat3668.

[26] V. Beermann, M. Gocyla, S. Kühl, E. Padgett, H. Schmies, M. Goerlin, N. Erini, M. Shviro, M. Heggen, R.E. Dunin-Borkowski, D.A. Muller, P. Strasser, Tuning the Electrocatalytic oxygen reduction reaction activity and stability of shape-controlled Pt–Ni nanoparticles by thermal annealing – elucidating the surface atomic structural and compositional changes, J. Am. Chem. Soc. 139 (2017) 16536–16547, https://doi.org/10.1021/jacs.7b06846.

[27] J. Li, S. Sharma, X. Liu, Y.-T. Pan, J.S. Spendelow, M. Chi, Y. Jia, P. Zhang, D. A. Cullen, Z. Xi, H. Lin, Z. Yin, B. Shen, M. Muzzio, C. Yu, Y.S. Kim, A.A. Peterson, K.L. More, H. Zhu, S. Sun, Hard-magnet L10-CoPt nanoparticles advance fuel cell catalysis, Joule 3 (2019) 124–135, https://doi.org/10.1016/j.joule.2018.09.016.

[28] B.-A. Lu, T. Sheng, N. Tian, Z.-C. Zhang, C. Xiao, Z.-M. Cao, H.-B. Ma, Z.-Y. Zhou, S.-G. Sun, Octahedral PtCu alloy nanocrystals with high performance for oxygen reduction reaction and their enhanced stability by trace au, Nano Energy 33 (2017) 65–71, https://doi.org/10.1016/j.nanoen.2017.01.003.

[29] K. Wan, J. Wang, J. Zhang, B. Li, M. Chai, P. Ming, C. Zhang, Ligand carbonization in-situ derived ultrathin carbon shells enable high-temperature confinement synthesis of PtCo alloy catalysts for high-efficiency fuel cells, Chem. Eng. J. 482 (2024) 149060, https://doi.org/10.1016/j.cej.2024.149060.

[30] Y. Bian, H. Wang, Z. Gao, J. Hu, D. Liu, L. Dai, A facile approach to high-performance trifunctional electrocatalysts by substrate-enhanced electroless deposition of Pt/NiO/Ni on carbon nanotubes, Nanoscale 12 (2020) 14615–14625, https://doi.org/10.1039/D0NR03378B.

[31] M. Zhang, Q. Dai, H. Zheng, M. Chen, L. Dai, Novel MOF-derived co@N-C bifunctional catalysts for highly efficient Zn–air batteries and water splitting, Adv. Mater. 30 (2018), https://doi.org/10.1002/adma.201705431, 1705431.

[32] H. Rong, T. Zhan, Y. Sun, Y. Wen, X. Liu, H. Teng, ZIF-8 derived nitrogen, phosphorus and sulfur tri-doped mesoporous carbon for boosting electrocatalysis to oxygen reduction in universal pH range, Electrochim. Acta 318 (2019) 783–793, https://doi.org/10.1016/j.electacta.2019.06.122.

[33] X. Hu, W. Zheng, M. Wu, L. Chen, S. Chen, Composites of metal-organic frameworks (MOFs) and LDHs for energy storage and environmental applications: fundamentals, progress, and perspectives, Sustain. Mater. Technol. 37 (2023) e00691, https://doi.org/10.1016/j.susmat.2023.e00691.

[34] S. Zhao, C. Wang, L. Cai, Y. Chen, W. Sun, Z. Zhu, A gasification strategy to anchor Fe, Ni dual-sites on biomass-derived N, P co-doped porous carbon as an efficient bifunctional catalyst for Zn-air batteries, Sustain. Mater. Technol. 40 (2024) e00875, https://doi.org/10.1016/j.susmat.2024.e00875.

[35] W. Xia, A. Mahmood, R. Zou, Q. Xu, Metal–organic frameworks and their derived nanostructures for electrochemical energy storage and conversion, Energy Environ. Sci. 8 (2015) 1837–1866, https://doi.org/10.1039/C5EE00762C.

[36] J. Wang, G. Han, L. Wang, L. Du, G. Chen, Y. Gao, Y. Ma, C. Du, X. Cheng, P. Zuo, G. Yin, ZIF-8 with ferrocene encapsulated: a promising precursor to single-atom Fe embedded nitrogen-doped carbon as highly efficient catalyst for oxygen Electroreduction, Small 14 (2018), https://doi.org/10.1002/smll.201704282, 1704282.

[37] L. Liang, H. Jin, H. Zhou, B. Liu, C. Hu, D. Chen, Z. Wang, Z. Hu, Y. Zhao, H.-W. Li, D. He, S. Mu, Cobalt single atom site isolated Pt nanoparticles for efficient ORR and HER in acid media, Nano Energy 88 (2021) 106221, https://doi.org/10.1016/j.nanoen.2021.106221.

[38] J. Li, S. Hu, Y. Li, X. Fan, F. Zhang, G. Zhang, W. Peng, Pyrrolic N anchored atomic Ni–N3–C catalyst for highly effective electroreduction of CO2 into CO, Carbon N. Y. 206 (2023) 62–71, https://doi.org/10.1016/j.carbon.2023.02.007.

[39] L. Lyu, X. Hu, S. Lee, W. Fan, G. Kim, J. Zhang, Z. Zhou, Y.-M. Kang, Oxygen reduction kinetics of Fe–N–C single atom catalysts boosted by Pyridinic N vacancy for temperature-adaptive Zn–air batteries, J. Am. Chem. Soc. 146 (2024) 4803–4813, https://doi.org/10.1021/jacs.3c13111.

[40] C. Lv, R. Xue, J. Zhang, X. Chen, D.-L. Chen, F.-F. Wang, F. Zhang, W. Zhu, Theoretical evidence on pyridinic nitrogen in N, S-coordinated co single atom catalyst as dominant active site promoting H2 cleavage, H diffusion, and hydrogenation activity, J. Catal. 435 (2024) 115549, https://doi.org/10.1016/j.jcat.2024.115549.

[41] T. Duc Le, M.J. Ahemad, D.-S. Kim, B.-H. Lee, G.-J. Oh, G.-S. Shin, L. R. Nagappagari, V. Dao, T. Van Tran, Y.-T. Yu, Synergistic effect of Pt-Ni dual

single-atoms and alloy nanoparticles as a high-efficiency electrocatalyst to minimize Pt utilization at cathode in polymer electrolyte membrane fuel cells, J. Colloid Interface Sci. 634 (2023) 930–939, https://doi.org/10.1016/j.jcis.2022.12.061.
[42] X.-W. Lv, W.-W. Tian, Z.-Y. Yuan, Recent advances in high-efficiency Electrocatalytic water splitting systems, Electrochem. Energy Rev. 6 (2023) 23, https://doi.org/10.1007/s41918-022-00159-1.
[43] C. Van Nguyen, Y.-T. Liao, T.-C. Kang, J.E. Chen, T. Yoshikawa, Y. Nakasaka, T. Masuda, K.C.-W. Wu, A metal-free, high nitrogen-doped nanoporous graphitic carbon catalyst for an effective aerobic HMF-to-FDCA conversion, Green Chem. 18 (2016) 5957–5961, https://doi.org/10.1039/C6GC02118B.
[44] C. Van Nguyen, S. Lee, Y.G. Chung, W.-H. Chiang, K.C.-W. Wu, Synergistic effect of metal-organic framework-derived boron and nitrogen heteroatom-doped three-dimensional porous carbons for precious-metal-free catalytic reduction of nitroarenes, Appl. Catal. B Environ. 257 (2019) 117888, https://doi.org/10.1016/j.apcatb.2019.117888.
[45] Q. Huo, J. Li, X. Qi, G. Liu, X. Zhang, B. Zhang, Y. Ning, Y. Fu, J. Liu, S. Liu, Cu, Zn-embedded MOF-derived bimetallic porous carbon for adsorption desulfurization, Chem. Eng. J. 378 (2019) 122106, https://doi.org/10.1016/j.cej.2019.122106.
[46] P. Tan, Y. Jiang, L.-B. Sun, X.-Q. Liu, K. AlBahily, U. Ravon, A. Vinu, Design and fabrication of nanoporous adsorbents for the removal of aromatic sulfur compounds, J. Mater. Chem. A 6 (2018) 23978–24012, https://doi.org/10.1039/C8TA09184F.
[47] Y. Wang, J. Zhou, Y. He, Y. Liu, C. Xu, Highly performed nitrogen-doped porous carbon electrocatalyst for oxygen reduction reaction prepared by a simple and slight regulation in hydrolyzing process of ZIF-8, J. Solid State Chem. 302 (2021) 122415, https://doi.org/10.1016/j.jssc.2021.122415.
[48] K. Zhou, B. Mousavi, Z. Luo, S. Phatanasri, S. Chaemchuen, F. Verpoort, Characterization and properties of Zn/co zeolitic imidazolate frameworks vs. ZIF-8 and ZIF-67, J. Mater. Chem. A 5 (2017) 952–957, https://doi.org/10.1039/C6TA07860E.
[49] W. Xue, Q. Zhou, F. Li, B.S. Ondon, Zeolitic imidazolate framework-8 (ZIF-8) as robust catalyst for oxygen reduction reaction in microbial fuel cells, J. Power Sources 423 (2019) 9–17, https://doi.org/10.1016/j.jpowsour.2019.03.017.
[50] M. Li, Z. Hu, H. Li, W. Zhao, W. Zhou, Q. Yang, S. Hu, Pt–Ni alloy nanoparticles via high-temperature shock as efficient Electrocatalysts in the oxygen reduction reaction, ACS Appl. Nano Mater. 5 (2022) 8243–8250, https://doi.org/10.1021/acsanm.2c01341.
[51] W. Guo, X. Gao, M. Zhu, C. Xu, X. Zhu, X. Zhao, R. Sun, Z. Xue, J. Song, L. Tian, J. Xu, W. Chen, Y. Lin, Y. Li, H. Zhou, Y. Wu, A closely packed Pt1.5Ni1−x/Ni–N–C hybrid for relay catalysis towards oxygen reduction, Energy Environ. Sci. (2023), https://doi.org/10.1039/D2EE02381D.
[52] T.D. Le, D. Van Dao, G. Adilbish, Y.-T. Yu, Electrophoretic deposition of carbon-supported octahedral Pt–Ni alloy nanoparticle catalysts for cathode in polymer electrolyte membrane fuel cells, Int. J. Hydrog. Energy 47 (2022) 1833–1844, https://doi.org/10.1016/j.ijhydene.2021.10.132.
[53] A. Das, S. Pisana, B. Chakraborty, S. Piscanec, S.K. Saha, U.V. Waghmare, K. S. Novoselov, H.R. Krishnamurthy, A.K. Geim, A.C. Ferrari, A.K. Sood, Monitoring dopants by Raman scattering in an electrochemically top-gated graphene transistor, Nat. Nanotechnol. 3 (2008) 210–215, https://doi.org/10.1038/nnano.2008.67.
[54] M. Xiao, Y. Jiao, B. Luo, S. Wang, P. Chen, M. Lyu, A. Du, L. Wang, Understanding the roles of carbon in carbon/g-C3N4 based photocatalysts for H2 evolution, Nano Res. 16 (2023) 4539–4545, https://doi.org/10.1007/s12274-021-3897-7.
[55] Y. Zhang, Y. Jia, M. Li, L. Hou, Influence of the 2-methylimidazole/zinc nitrate hexahydrate molar ratio on the synthesis of zeolitic imidazolate framework-8 crystals at room temperature, Sci. Rep. 8 (2018) 9597, https://doi.org/10.1038/s41598-018-28015-7.
[56] X. Chen, X. An, L. Tang, T. Chen, G. Zhang, Confining platinum clusters in ZIF-8-derived porous N-doped carbon arrays for high-performance hydrogen evolution reaction, Chem. Eng. J. 429 (2022) 132259, https://doi.org/10.1016/j.cej.2021.132259.
[57] P. Lu, M. Yin, J. Chen, Q. Wang, C. Ye, T. Qiu, ZiF-8-derived P, N-co-doped hierarchical carbon: synergistic and high-efficiency desulfurization adsorbents, Chem. Eng. J. 429 (2022) 132458, https://doi.org/10.1016/j.cej.2021.132458.
[58] X. Xie, L. Shang, X. Xiong, R. Shi, T. Zhang, Fe single-atom catalysts on MOF-5 derived carbon for efficient oxygen reduction reaction in proton exchange membrane fuel cells, Adv. Energy Mater. 12 (2022), https://doi.org/10.1002/aenm.202102688, 2102688.
[59] N. Wang, K. Komvopoulos, Incidence angle effect of energetic carbon ions on deposition rate, topography, and structure of ultrathin amorphous carbon films deposited by filtered cathodic vacuum arc, IEEE Trans. Magn. 48 (2012) 2220–2227, https://doi.org/10.1109/TMAG.2012.2190295.
[60] R.J. Yeo, E. Rismani, N. Dwivedi, D.J. Blackwood, H.R. Tan, Z. Zhang, S. Tripathy, C.S. Bhatia, Bi-level surface modification of hard disk media by carbon using filtered cathodic vacuum arc: reduced overcoat thickness without reduced corrosion performance, Diam. Relat. Mater. 44 (2014) 100–108, https://doi.org/10.1016/j.diamond.2014.02.011.
[61] B.K. Pathem, X.-C. Guo, F. Rose, N. Wang, K. Komvopoulos, E. Schreck, B. Marchon, Carbon overcoat oxidation in heat-assisted magnetic recording, IEEE Trans. Magn. 49 (2013) 3721–3724, https://doi.org/10.1109/TMAG.2012.2236645.
[62] N. Dwivedi, E. Rismani-Yazdi, R.J. Yeo, P.S. Goohpattader, N. Satyanarayana, N. Srinivasan, B. Druz, S. Tripathy, C.S. Bhatia, Probing the role of an atomically thin SiNx interlayer on the structure of ultrathin carbon films, Sci. Rep. 4 (2014) 5021, https://doi.org/10.1038/srep05021.
[63] S. Biniak, G. Szymański, J. Siedlewski, A. Świątkowski, The characterization of activated carbons with oxygen and nitrogen surface groups, Carbon N. Y. 35 (1997) 1799–1810, https://doi.org/10.1016/S0008-6223(97)00096-1.
[64] P. Song, Y. Zhang, J. Pan, L. Zhuang, W. Xu, Cheap carbon black-based high-performance electrocatalysts for oxygen reduction reaction, Chem. Commun. 51 (2015) 1972–1975, https://doi.org/10.1039/C4CC07677J.
[65] J. Xu, C. Zhang, H. Liu, J. Sun, R. Xie, Y. Qiu, F. Lü, Y. Liu, L. Zhuo, X. Liu, J. Luo, Amorphous MoOX-stabilized single platinum atoms with ultrahigh mass activity for acidic hydrogen evolution, Nano Energy 70 (2020) 104529, https://doi.org/10.1016/j.nanoen.2020.104529.
[66] R. Brandiele, C. Durante, M. Zerbetto, N. Vicentini, T. Kosmala, D. Badocco, P. Pastore, G.A. Rizzi, A.A. Isse, A. Gennaro, Probing the correlation between Pt-support interaction and oxygen reduction reaction activity in mesoporous carbon materials modified with Pt-N active sites, Electrochim. Acta 277 (2018) 287–300, https://doi.org/10.1016/j.electacta.2018.04.182.
[67] C.H. Choi, H.-K. Lim, M.W. Chung, J.C. Park, H. Shin, H. Kim, S.I. Woo, Long-range Electron transfer over graphene-based catalyst for high-performing oxygen reduction reactions: importance of size, N-doping, and metallic impurities, J. Am. Chem. Soc. 136 (2014) 9070–9077, https://doi.org/10.1021/ja5033474.
[68] Y. Wang, J. Mao, X. Meng, L. Yu, D. Deng, X. Bao, Catalysis with two-dimensional materials confining single atoms: concept, design, and applications, Chem. Rev. 119 (2019) 1806–1854, https://doi.org/10.1021/acs.chemrev.8b00501.
[69] G. Chen, M. Li, K.A. Kuttiyiel, K. Sasaki, F. Kong, C. Du, Y. Gao, G. Yin, R.R. Adzic, Evaluation of oxygen reduction activity by the thin-film rotating disk electrode methodology: the effects of Potentiodynamic parameters, Electrocatalysis 7 (2016) 305–316, https://doi.org/10.1007/s12678-016-0309-y.
[70] H. Sun, M. Wang, S. Zhang, S. Liu, X. Shen, T. Qian, X. Niu, J. Xiong, C. Yan, Boosting oxygen dissociation over bimetal sites to facilitate oxygen reduction activity of zinc-air battery, Adv. Funct. Mater. 31 (2021), https://doi.org/10.1002/adfm.202006533, 2006533.
[71] J. Chen, H. Li, C. Fan, Q. Meng, Y. Tang, X. Qiu, G. Fu, T. Ma, Dual single-atomic Ni-N4 and Fe-N4 sites constructing Janus hollow graphene for selective oxygen Electrocatalysis, Adv. Mater. 32 (2020), https://doi.org/10.1002/adma.202003134, 2003134.
[72] H. Liu, J. Zhao, X. Li, Controlled synthesis of carbon-supported Pt-based Electrocatalysts for proton exchange membrane fuel cells, Electrochem. Energy Rev. 5 (2022) 13, https://doi.org/10.1007/s41918-022-00173-3.
[73] Z. Chen, D. Cummins, B.N. Reinecke, E. Clark, M.K. Sunkara, T.F. Jaramillo, Core–shell MoO3–MoS2 nanowires for hydrogen evolution: a functional Design for Electrocatalytic Materials, Nano Lett. 11 (2011) 4168–4175, https://doi.org/10.1021/nl2020476.
[74] N. Cheng, S. Stambula, D. Wang, M.N. Banis, J. Liu, A. Riese, B. Xiao, R. Li, T. K. Sham, L.M. Liu, G.A. Botton, X. Sun, Platinum single-atom and cluster catalysis of the hydrogen evolution reaction, Nat. Commun. 7 (2016) 13638.
[75] P. Xiao, M.A. Sk, L. Thia, X. Ge, R.J. Lim, J.-Y. Wang, K.H. Lim, X. Wang, Molybdenum phosphide as an efficient electrocatalyst for the hydrogen evolution reaction, Energy Environ. Sci. 7 (2014) 2624–2629, https://doi.org/10.1039/C4EE00957F.
[76] A. Kumar, S. Parvin, R.K. Das, S. Bhattacharyya, Comprehensive and high-throughput electrolysis of water and urea by 3–5 nm nickel and copper coordination polymers, Chem. Asian J. 16 (2021) 3444–3452, https://doi.org/10.1002/asia.202100916.
[77] F. Xiao, Q. Wang, G.-L. Xu, X. Qin, I. Hwang, C.-J. Sun, M. Liu, W. Hua, H. Wu, S. Zhu, J.-C. Li, J.-G. Wang, Y. Zhu, D. Wu, Z. Wei, M. Gu, K. Amine, M. Shao, Atomically dispersed Pt and Fe sites and Pt–Fe nanoparticles for durable proton exchange membrane fuel cells, Nat. Catal. 5 (2022) 503–512, https://doi.org/10.1038/s41929-022-00796-1.
[78] L. Yu, D. Deng, X. Bao, Chain mail for catalysts, Angew. Chem. Int. Ed. 59 (2020) 15294–15297, https://doi.org/10.1002/anie.202007604.
[79] J. Deng, D. Deng, X. Bao, Robust catalysis on 2D materials encapsulating metals: concept, application, and perspective, Adv. Mater. 29 (2017), https://doi.org/10.1002/adma.201606967, 1606967.